The 27 February 2022 Lop Nor Earthquake: Detectability, Location, and Discrimination

Steven J. Gibbons[*1] , Esteban J. Chaves[2] , and Mark Fisk[3]

Abstract

A seismic event with m_b 4.8 (M_w 4.2) was detected close to the Chinese Lop Nor nuclear test site on 27 February 2022. Waveforms recorded at regional and far regional distances in central Asia indicate greater likeness with previous earthquakes in the region than with historical nuclear tests. We investigate signal-to-noise ratio (SNR) at regional and global stations, and find the best signals in central Asia and Alaska. Lower SNR at stations in China, Europe, and Australia is likely related to the radiation pattern. A joint probabilistic location of the 2022 event and well-constrained historical nuclear tests indicates an epicenter near 41.88° N and 88.10° E, about 25 km northwest of the tunnel portion of the test site. A moment tensor inversion using high-quality regional signals indicates a nearly deviatoric source with a 72% double couple and a reverse fault mechanism. The centroid depth is 20–25 km, consistent with depth phases recorded in Alaska. The observed faulting geometry and source composition for the 2022 Lop Nor event is consistent with previous earthquakes in the region and the spatial alignment of local geomorphological features, indicating tectonic and not anthropogenic origin.

Introduction

On 27 February 2022, the National Earthquake Information Center (NEIC) at the U.S. Geological Survey (USGS) reported a seismic event at 19:52:16 UTC with magnitude m_b 4.8 within 30 km of China's Lop Nor nuclear test site. Recent earthquakes in the region are well documented (e.g., Selby *et al.*, 2005; Fox *et al.*, 2012) but accurate location, and unequivocal identification as an earthquake at a depth that excludes anthropogenic activity, is fundamental to forensic seismology. Location and discrimination are helped significantly by recordings of both earthquakes and explosions on still operating open seismic stations (e.g., Kohl *et al.*, 2002). The nuclear test locations are well constrained through precision seismology and satellite data (Fisk, 2002; Waldhauser *et al.*, 2004) and modern, contextual, location methods (e.g., Richards *et al.*, 2006; Myers *et al.*, 2007) exploiting ground truth (GT) locations should validate or improve on conventional network location estimates. Similarly, differences in temporal and spectral characteristics of waveforms have provided a basis for discrimination (e.g., Levshin and Ritzwoller, 1995; Cong *et al.*, 1996; Korrat *et al.*, 2008).

Figure 1a,b shows signals from the 27 February event on two far-regional stations with an open data archive extending back to the time of explosive nuclear testing at Lop Nor: AAK (Ala Archa, Kyrgyzstan) and NIL (Nilore, Pakistan). The signals at these two stations are very different from each other. At AAK, the *Pn* arrival is followed by high-amplitude coda with dominant amplitude in the *Lg* part of the signal. At NIL, the dominant amplitudes correspond to the *Pn* and *Sn* arrivals. There is no clear *Sn* arrival on the AAK vertical component, and there is no clear *Lg* visible at NIL. Figure 1 also displays signals at these two stations from three other events: a tunnel nuclear explosion

1. Norwegian Geotechnical Institute, Oslo, Norway, https://orcid.org/0000-0002-7822-0244 (SJG); 2. Volcanological and Seismological Observatory of Costa Rica, Universidad Nacional, Heredia, Costa Rica, https://orcid.org/0000-0002-5724-1513 (EJC); 3. Leidos Dynetics-Linc, Applied Science Division, Arlington, Virginia, U.S.A., https://orcid.org/0000-0002-1149-3854 (MF)

*Corresponding author: steven.gibbons@ngi.no
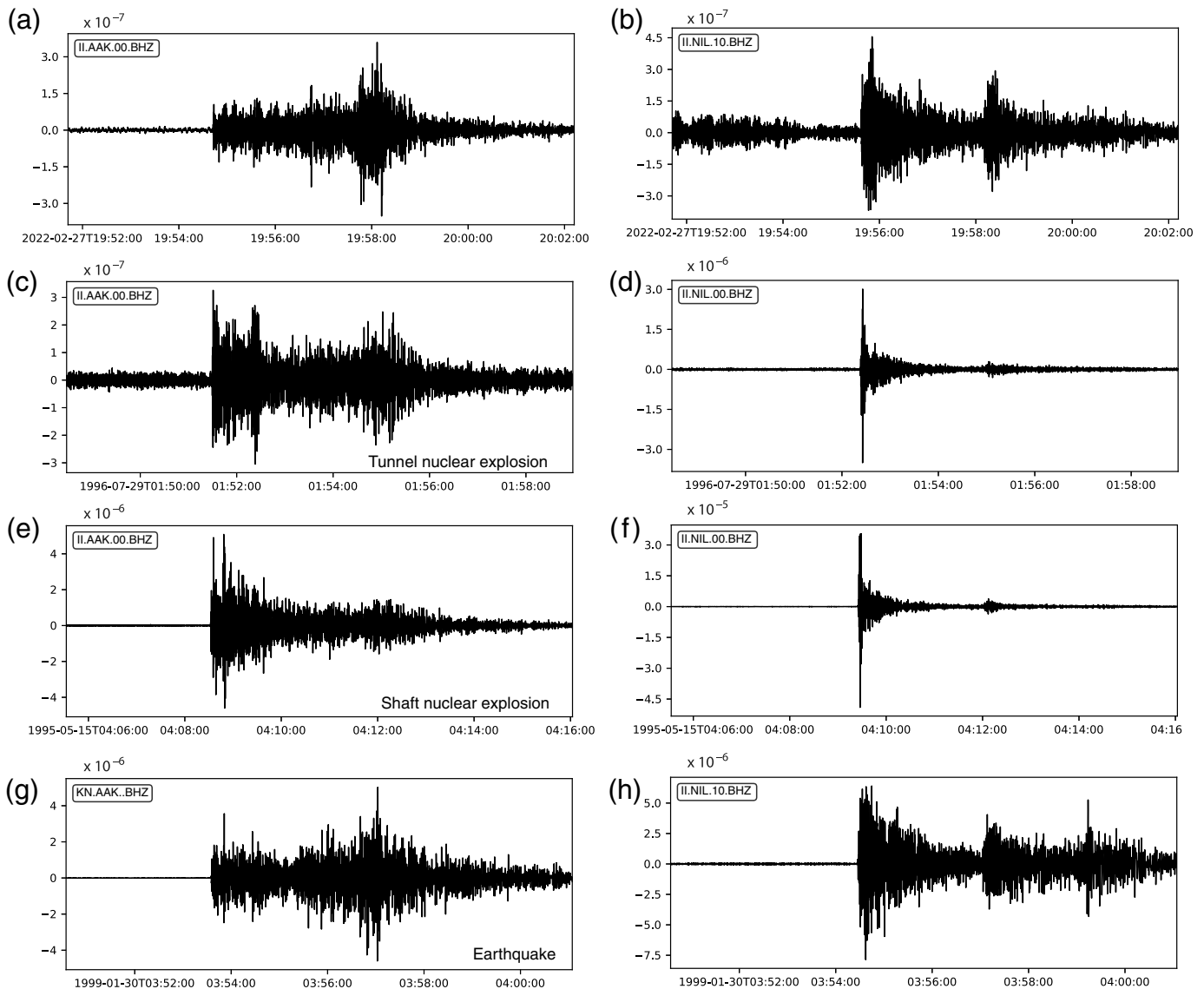
Figure 1. Recordings of the 27 February 2022 Lop Nor event on stations II.AAK/KN.AAK: (panel a: distance 10.2°, azimuth 278°) and II.NIL (panel b: distance 14.4°, azimuth 240°). Panels (c) and (d) show the corresponding signals from the 29 July 1996 tunnel nuclear test, panels (e) and (f) show the corresponding traces from 15 May 1995 shaft nuclear test, and panels (g) and (h) from the 30 January 1999 earthquake. The instrument responses have been removed and a 1.0–4.5 Hz band-pass filter applied to all traces. Each waveform is aligned according to the first *P*-arrival time at AAK (Ala Archa, Kyrgyzstan), and all the traces are scaled individually, displaying velocity in meter/second.

(panels c,d), a shaft nuclear explosion (e,f), and an earthquake (g,h). After inspecting corresponding waveforms from many more events, it was deemed that these three previous events were sufficiently representative of the classes they were chosen from. At AAK, the relationship between *Pn* and *Lg* is rather different for the four events. Both the nuclear explosions (Fig. 1c,e) have higher *Pn/Lg* ratios than the other two events (panels a,f). However, the *Pn/Lg* ratio is higher for the shaft explosion than for the tunnel explosion. The 2022 signal bears greater similarity to the tunnel explosion signal (panel c) than the shaft explosion signal (panel e). The differences could be both source and location related. The signals at NIL show greater differences between the nuclear tests (panels d,f) and the other events (panels b,h). For the nuclear tests, the *Pn* amplitude at NIL is an order of

magnitude greater than the *Sn* amplitude. For the other events, *Pn* and *Sn* have comparable amplitudes. For this frequency band, the *Sn/Pn* ratio at NIL is marginally higher for the 2022 event (panel b) than for the 1999 earthquake (panel h).

Here, we have three principal aims: (1) To examine global detectability of the 2022 event with its consequences for future seismic monitoring of the region; (2) to exploit historical seismic events and modern earthquake location methods to better constrain the 2022 event epicenter; and (3) to better constrain the source and focal depth using regional and teleseismic data. We note that the signals on open stations with the highest signal-to-noise ratio (SNR) are IC.WMQ and G.WUS, both on Chinese territory. We exploit these signals for moment tensor inversion and depth determination; but note that, although both were operational in the 1990s, they were switched off at the times of Chinese nuclear tests, and no data from these stations is available for comparison. This is additional motivation for exploiting teleseismic data for depth estimation. The following three sections address aims (1), (2), and (3), in turn.

Seismic Recordings and Global Detectability

The NEIC (USGS) event information page (see Data and Resources) provides both phase arrival times and amplitudes, periods, and magnitudes estimated from each of the stations used. Figure 2a displays a histogram of these m_b estimates. Although the range extends from 3.8 to 5.4, the distribution has a clear maximum at m_b 4.7–4.8. Although the reviewed solution from the International Seismological Center (ISC) is not yet available (it is anticipated around April 2024), searching the ISC bulletin for events within appropriate temporal and geographical windows provides a preliminary summary of origins and phase readings from different agencies. The output from a search performed on 2 April 2022 is saved with the dataset associated with this paper on Xenodo (see Data and Resources). Among these arrivals is a set of m_b estimates from a different set of stations, measured by GeoForschungsZentrum (GFZ), Potsdam. The corresponding histogram (Fig. 2b) shows a slightly different distribution but with range and averages largely consistent with the NEIC estimates.
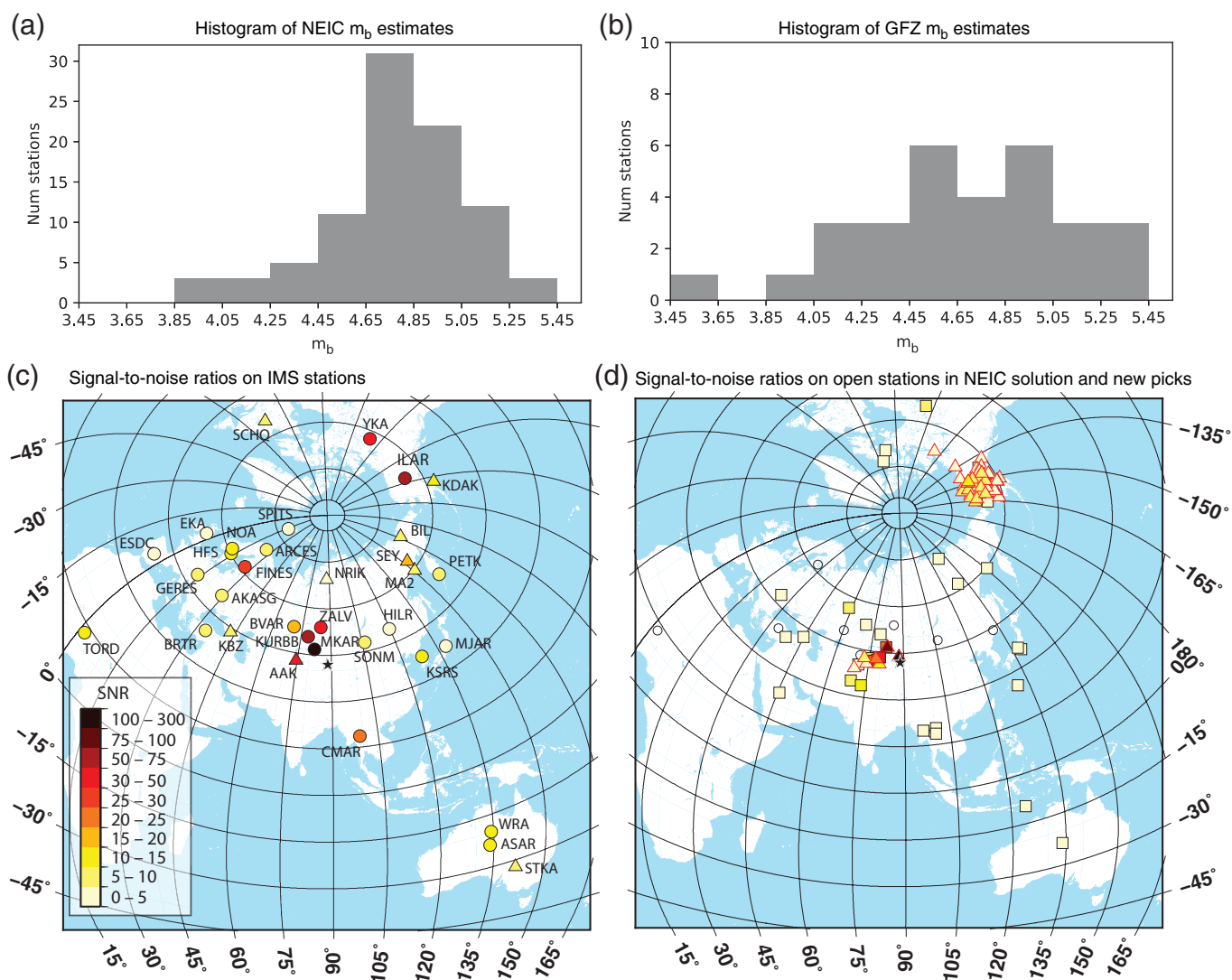
Also in the preliminary ISC bulletin are phase readings provided by the International Data Center (IDC) for the Comprehensive Nuclear-Test-Ban Treaty Organization (CTBTO). These arrivals are particularly useful for several reasons. First, they are made exclusively from stations of the International Monitoring System (IMS), which includes some of the most sensitive seismic stations on Earth, many of which are seismic arrays and many of which provide data not openly accessible to scientists outside the CTBTO system. Second, they are frequently associated with rich metadata including backazimuth and apparent velocity—information from the IDC array-

processing algorithms. Third, arrivals are typically listed with the SNR measured on the optimal traces (usually beams formed with appropriate steering parameters and filtered in optimal frequency bands). The SNR can be a proxy for how accurately we can read an arrival time and for the detection threshold for events in a given source region on a given station.

Figure 2c displays the SNR at IMS stations, as reported to the ISC. These values can indicate the propagation efficiency along a given path (e.g., Kværna and Ringdal, 2013) but are also sensitive to radiation pattern (e.g., Schweitzer and Kvaerna, 1999) and can be influenced by station geometry, location, and array properties (e.g., Kværna et al., 2021). They will also be subject to varying noise levels. Unsurprisingly, the IMS arrays in Central Asia record a high SNR; likewise the ILAR array in Alaska. Other sensitive array stations such as WRA and ASAR in Australia and GERES and ESDC in Europe record relatively low SNR. As these stations recorded Lop Nor nuclear tests well, this is likely a radiation pattern effect. These SNR values can hint how well nearby three-component stations are likely to detect an event. If a sensitive array station offers an SNR of 4 on an optimal beam, nearby single stations (without the array's noise suppression) are unlikely to record a usable signal (e.g., Ringdal, 1990).

Figure 2d displays, using colored squares, single-channel SNR measurements on those stations in the NEIC/USGS solution that are openly available from the Incorporated Research Institutions for Seismology (IRIS). In addition, all vertical component traces available via IRIS were searched for clear signal onsets near the predicted P-wave arrival times. Those stations not in the NEIC/USGS solutions, for which a satisfactory signal was observed, are displayed with colored triangles. The SNR displayed in Figure 2d is the ratio of the average signal envelope in the 2 s following the P arrival to the average signal envelope in the 2 s prior, with all waveforms band-pass filtered in the 1–4 Hz band. The SNR values displayed in Figure 2d are not directly comparable with those displayed in Figure 2c but are internally consistent.

IC.WMQ and G.WUS are the only open stations in China with clear signal onsets. The remaining stations of the IC network show very poor signal onsets that were not deemed useful for constraining the event location. There are few regions in the world where very high-quality arrivals were observed that had not already been exploited in the NEIC/USGS solution. A notable exception is northern Alaska where many stations of the AK and IM networks (many formerly in the USArray Transportable Array) display exceptionally impulsive and high
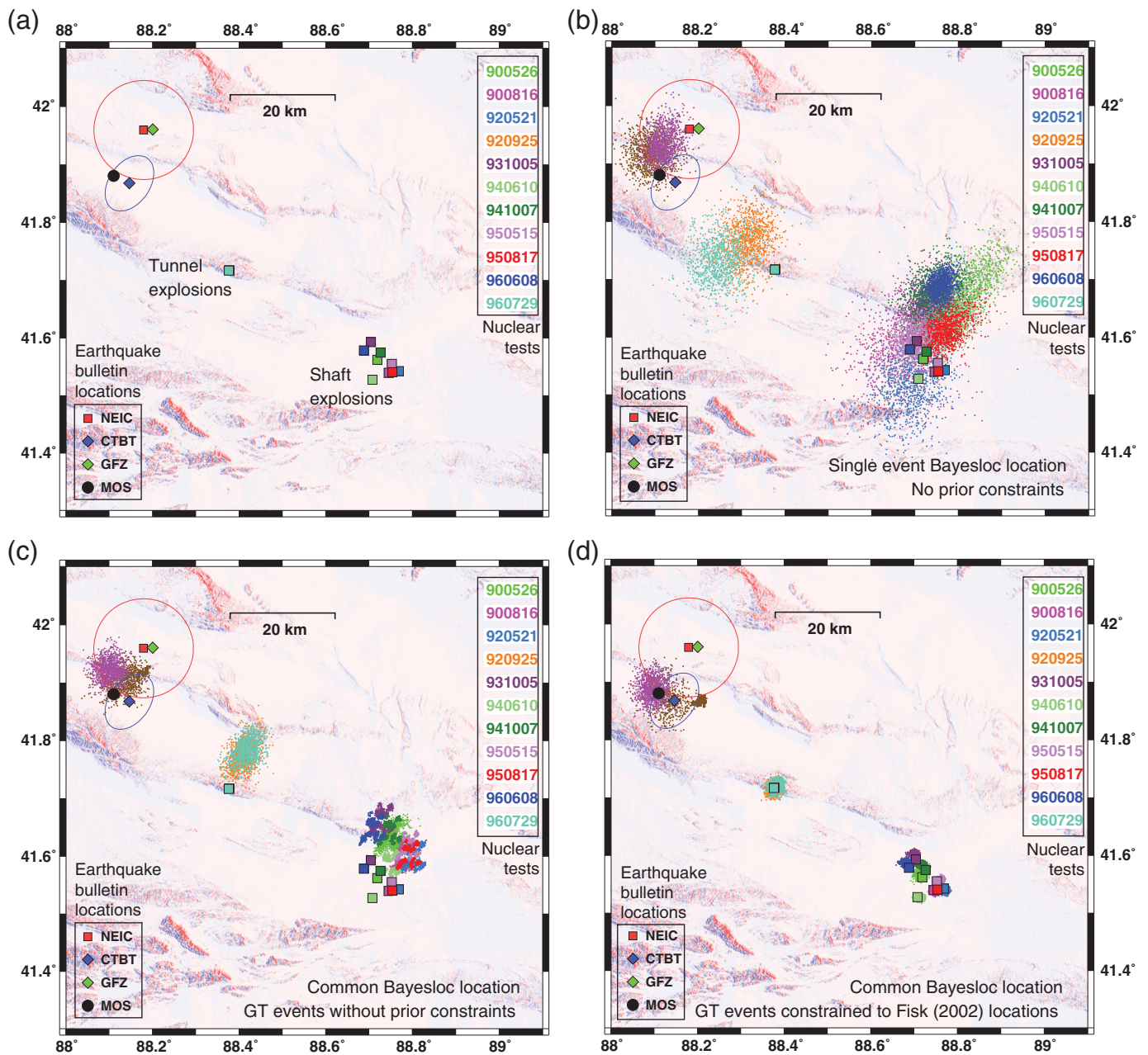
Figure 2. m_b estimates and detectability at global seismic stations for the 27 February 2022 Lop Nor event. (a,b) Histograms of single-station m_b for the National Earthquake Information Center (NEIC; U.S. Geological Survey [USGS]) and GeoForschungsZentrum, Potsdam, respectively. Note that panels (a) and (b) have different vertical scales with far fewer stations contributing to panel (b). (c) The signal-to-noise ratio (SNR) reported for first P waves at arrays (circles) and three-component stations (triangles) of the International Monitoring System, extracted from the bulletin of the International Seismological Center (ISC, 2022). (d) The SNR measured (this study) at the P-wave arrival times given in the NEIC/USGS bulletin (squares) and at open stations not used in the NEIC/USGS bulletin (triangles). Empty circles in panel (d) indicate stations used in the NEIC/USGS bulletin for which the waveform data is not open. The black star in panels (c) and (d) represent the epicenter of the 27 February 2022, Lop Nor event.

SNR signals. These relatively new stations, together with the Alaskan seismic arrays, likely offer a low detection threshold for seismic events at Lop Nor.

Location

Figure 3a shows the location estimates from four different agencies as published by the ISC online bulletin together with the locations of the 11 most recent Lop Nor underground nuclear tests from Fisk (2002). The nuclear tests are in two distinct groups. At 41.72° N and 88.38° E (25 km southeast of the 27 February 2022 event) we have two tunnel explosions: 920925 and 960729. Their locations are indistinguishable at the scales used in this plot. The nine shaft explosions are located about 25 km to the southeast of here, within 10 km of each other. As of 2 April 2022, the ISC bulletin had epicenters

Figure 3. Location estimates for the 27 February 2022 Lop Nor event relative to underground nuclear explosions located using precision seismology and satellite imagery (Fisk, 2002). (a) The square symbols indicate the locations of the nuclear tests according to color, and the remaining symbols indicate the location estimates for the 2022 event reported by the agencies, as indicated obtained from the USGS and ISC websites. (b) Bayesloc location estimates for the 12 events solved individually. (c) The same set of events solved simultaneously without constraining the ground truth (GT) events laterally. (d) The same set of events solved simultaneously with the GT events fixed to the locations specified in Fisk (2002). Two clouds of points are displayed for the 2022 event: using NEIC (USGS) arrivals only (brown) and using the selected superset of arrivals from the ISC bulletin and new arrival picks (magenta). The brown and magenta points are solved for in separate calculations. The clouds for the nuclear tests displayed are those calculated using the superset of arrivals (magenta points).

reported by four different agencies: the NEIC/USGS, GFZ Potsdam, the Geophysical Survey of the Russian Academy of Sciences in Moscow (MOS), and the IDC (CTBTO). Lateral uncertainty estimates are only provided for the NEIC/USGS and IDC/CTBTO solutions. Topography on the map is indicated by a hillshade map obtained from the LiCSAR database (Lazeckỳ *et al.*, 2020; see Data and Resources), chosen for the high resolution and the fact that this map emphasizes steepness of the topography rather than the elevation itself.

We locate the 27 February 2022 event using the Bayesloc program (Myers *et al.*, 2007, 2009), because it allows us to calculate and visualize probability distributions of hypocenter estimates under different conditions. Bayesloc calculates probability distributions for corrections to travel-time estimates when clustered events are used, which can result in exceptionally precise relative location estimates even using only a 1D velocity model. An exceptional strength of Bayesloc is that source parameters from well-constrained events can be input as prior constraints, improving the accuracy of the absolute locations. This is the case for Lop Nor in which the 11 historical nuclear tests, recorded by many of the same stations that recorded the 2022 event, are constrained using both precision seismology and satellite imagery. Figure 3b–d displays two estimates for the 2022 event under different conditions regarding the GT nuclear events. The clouds of brown dots indicate epicenter estimates for the 2022 event using only the phase arrivals published in the NEIC/USGS solution. The clouds of magenta dots indicate epicenter estimates for the 2022 events using a superset of arrivals collected in the current study. All input to the Bayesloc program can be downloaded from the dataset associated with this article on Xenodo (see Data and Resources).

Although it is almost always advantageous to locate clustered seismic events simultaneously when using Bayesloc, events can be located individually. Figure 3b shows clouds of dots from 13 different runs of Bayesloc with distinct colors for each of the 11 nuclear tests and the two different sets of arrival times for the 27 February 2022 event. Each dot is a single sample of the joint probability distribution for an event epicenter in a Monte Carlo Markov Chain (MCMC). Each cloud displays the epicenters for the final 1000 iterations of a total of 40,000 for each of eight different MCMC threads for a given event and set of arrival times. The geographical extent of each cloud should provide an indication of the lateral uncertainty associated with the location estimate for that set of arrivals. Both clouds for the 2022 event fit inside circles with diameters

a little over 10 km, slightly north of the MOS and IDC/CTBT location estimates and slightly southwest of the NEIC/USGS and GFZ location estimates. The small offset of the cloud using NEIC arrivals from the NEIC-provided epicenter can be due to different weightings of the arrival times, differences in the location algorithms, or both. The clouds corresponding to the well-constrained nuclear explosions (together with their GT locations) indicate the confidence with which we can associate the extent of the clouds with the true location uncertainty. Where the clouds are significantly displaced from the GT locations, we infer a location bias that can result from arrival time measurements errors, travel-time prediction errors, or both. The displacement vectors between the cloud centroids and the GT locations are different for each event. Although many of the same stations record the different events, the sets of arrival times vary considerably. (Some events are constrained by many more arrival times than others.) The clouds for the two almost co-located tunnel explosions indicate rather different location estimates. We conclude from Figure 3b that the single-event Bayesloc clouds typically show a lateral spread of approximately 10 km and have up to 10 km location bias, with the direction of the bias differing from event to event.

In Figure 3c, we use exactly the same sets of arrivals used in Figure 3b but calculate the joint probability distributions for the different events simultaneously. It is only when solving for nearby events simultaneously that Bayesloc is able to solve for the corrections to travel-time estimates. There are two qualitative differences between the clouds from the joint locations in Figure 3c and the individual locations in Figure 3b. First, the spread of each cloud is significantly diminished. Second, the displacement vectors between the clouds for the nuclear tests and their GT locations is almost identical from event to event (the centroid of each cloud is about 8 km north–northeast of the corresponding GT location). We note that the MCMC clouds for the two almost co-located tunnel explosions are approximately the same, and the MCMC clouds for the nine shaft explosions follow closely the spatial pattern of the GT locations, just uniformly translated.

The calculations displayed in Figure 3d are identical to those in Figure 3c, except that the nuclear tests are constrained by prior conditions on their GT locations. The clouds for the nuclear tests collapse around the GT locations, and the clouds for the 2022 event migrate several km to the southwest. The resulting clouds (for the 2022 event) are almost co-located with the MOS and IDC/CTBTO epicenters.

Focal Mechanism and Discrimination

We apply a regional full-waveform moment tensor inversion (MT) to determine source composition and faulting geometry for the 2022 event. Second rank general moment tensor inversion is commonly used to obtain source mechanisms at teleseismic (e.g., Dziewonski *et al.*, 1981; Ekström *et al.*, 2005) and regional (Jost and Herrmann, 1989; Minson and Dreger, 2008) distances. We adopt the time-domain moment tensor (TDMT) inversion approach (Dreger and Helmberger, 1993), in which the seismic source is simplified by considering a spatial and temporal point source:

$$U_n(x, t) = M_{ij} \times G_{ni,j}(x, z, t), \tag{1}$$

with U_n the observed nth component of displacement, M_{ij} the scalar seismic moment tensor, and $G_{ni,j}$ the nth component Green's function for specific force couple orientations. Equation (1) is solved by least squares for a given source depth. We solved for the full seismic moment tensor, which is decomposed into the scalar seismic moment, a double couple (DC) moment tensor (defined by the strike, dip, and rake angles of both nodal planes), a compensated linear vector dipole (CLVD), and an isotropic (ISO) moment tensor. The full moment tensor decomposition is performed following Jost and Herrmann (1989) and is represented as percent DC, CLVD, and ISO. For each station, three-component waveform data are corrected for instrument response, integrated to displacement, and band-pass filtered using a Butterworth filter with corners at 0.02 and 0.05 Hz. The horizontal traces are rotated to the great circle path to give tangential and radial components. Green's functions are computed using a frequency–wave number integration algorithm (Saikia, 1994) for a 1D velocity model (here, the ak135 model: Kennett *et al.*, 1995) and filtered as with the data. To perform the MT inversion, we assume the epicenter location and determine the source depth, finding the solution with the largest variance reduction (VR), defined by

$$VR = \left[1 - \frac{\sum_i \sqrt{(\text{data}_i - \text{synth}_i)^2}}{\sqrt{(\text{data}_i)^2}} \right] \cdot 100, \tag{2}$$

in which data and synth represent the data and the Green's function time series of the ith station, respectively. Figure 4 shows the resulting moment tensor inversion for the 27 February 2022 event. The reverse thrust faulting mechanism with strike around 110° is consistent with the regional earthquake trend (Selby *et al.*, 2005) and is aligned with the geomorphological features visible in Figure 3.

The moment tensor inversion in Figure 4 relies on the closest open stations, including two on Chinese territory. We noted in the Seismic Recordings and Global Detectability section that many stations in northern Alaska recorded teleseismic *P*-wave arrivals with an exceptionally high SNR. Figure 5a displays 30 s long segments of data surrounding the *P* arrivals at 14 stations of The Alaska Regional Network (AK network). For each of these stations, a distinct burst of energy arrives about 8 s following the *P*-wave onset. On some stations (e.g., L18K) the second arrival appears to be a reversed polarity of the initial *P* arrival (a likely *pP* arrival); on other stations this is less clear. However, a time delay of 8 s at station IU.COLA in Alaska is consistent with an event at 41.88° N and 88.10° E at a depth of 25 km using the ak135 velocity model (Kennett *et al.*, 1995). At this location, using the ak135 model, depths of 20, 22, 24, 26, 28, and 30 km result in *pP*–*P* time delays at IU.COLA of 6.48, 7.05, 7.64, 8.19, 8.75, and 9.32 s, respectively. If we calculate *pP*–*P* time delays using the LLNL Earth3D model (Myers *et al.*, 2015), the corresponding times are 6.54, 7.13, 7.73, 8.30, 8.89, and 9.48 s, respectively. For both the velocity models, a depth of around 25 km is the most consistent with the 8 s arrival being a *pP* depth phase. Under the alternative hypothesis that the 8 s depth phase is *sP*, and with a low amplitude *pP* signal between the first *P* arrival and *sP*, the depth would be approximately 18 km. This depth is also consistent with the inversion displayed in Figure 4. Figure 5b shows the signal from the 2022 event on station IU.COLA together with the signal at nearby station IU.COL from the 15 May 1995 Lop Nor nuclear test. The 2022 event displays a secondary phase at 8 s, and the nuclear test signal does not. This means that the 8 s arrival is likely specific to the location and source mechanism of the 27 February 2022 event, rather than being a feature generic to events in that source region observed in Alaska.

Conclusions

A seismic event with m_b 4.8/M_w 4.2 occurred close to the Chinese Lop Nor nuclear test site on 27 February 2022. We describe its detectability both regionally and globally. It is the best recorded at regional and far-regional distances in central Asia and teleseismically in northern Alaska. The stations recently added to the AK network from the US Array Transportable Array (Busby and Aderhold, 2020) provide excellent recordings and, together with the four Alaskan array stations (ILAR, BCAR, BMAR, and IMAR), will likely sustain a
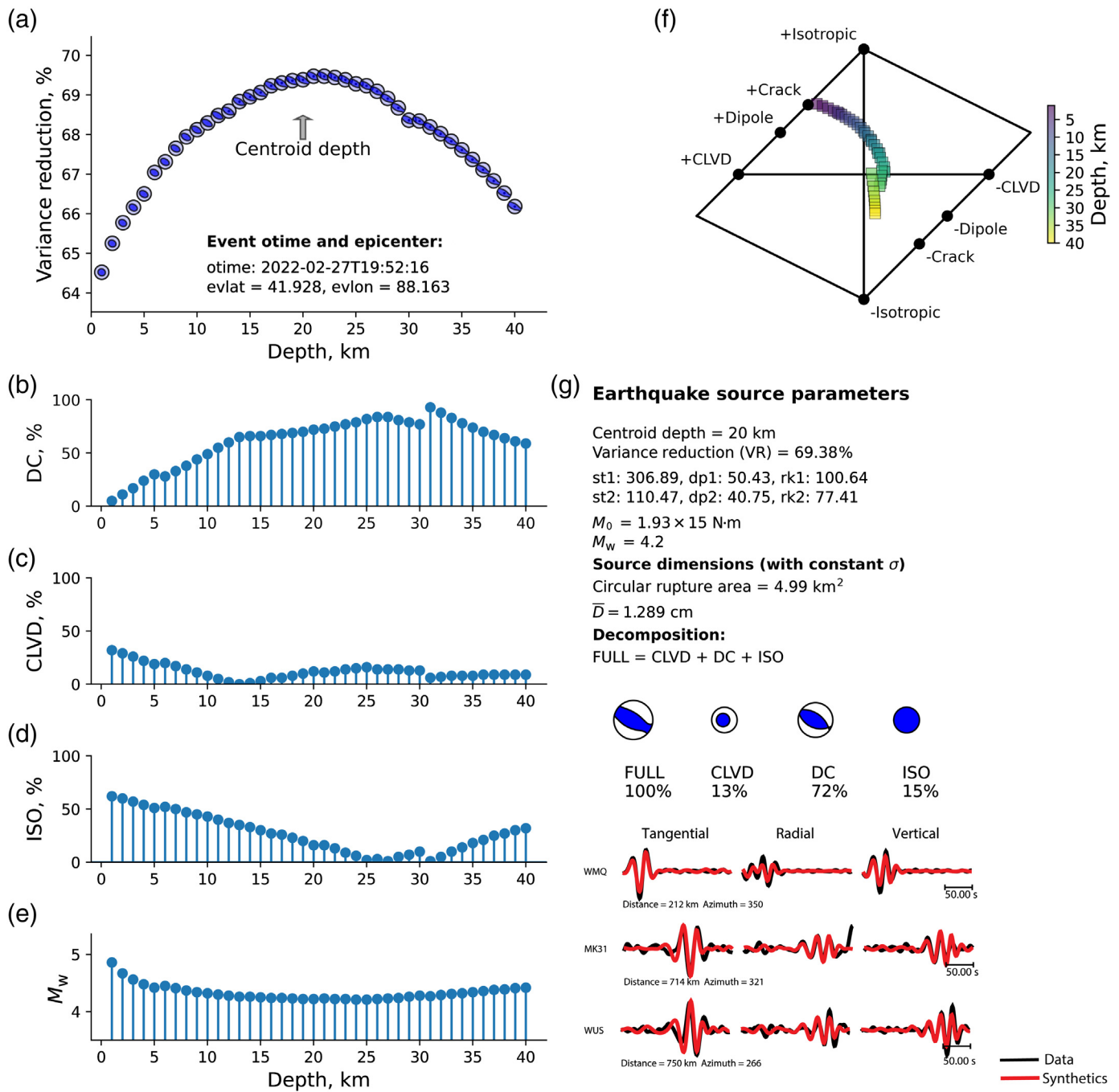
Figure 4. Full regional moment tensor inversion for the 27 February 2022, M_w 4.2 event. The waveform inversion is performed using stations WUS, WMQ, and MK31, from the French Global Network of Seismological Broadband stations: Geoscope (G), The New China Digital Seismograph Network (IC), and the International Miscellaneous stations (IM), respectively. (a) The variance reduction (VR) from the waveform fit as a function of depth. (b–d) The double couple (DC), compensated linear vector dipole (CLVD) and isotropic (ISO) components of the earthquake source as a function of depth. The magnitude variability with depth is similarly shown in panel (e). The source type plot (Hudson *et al.*, 1989) is represented in panel (f), whereas the source parameters, tensor decomposition, and waveform fit between the observed (black) and synthetic (red) seismograms are shown in panel (g). All waveforms can be accessed through International Federation of Digital Seismograph Networks (FDSN) web services.

(a)

(b)
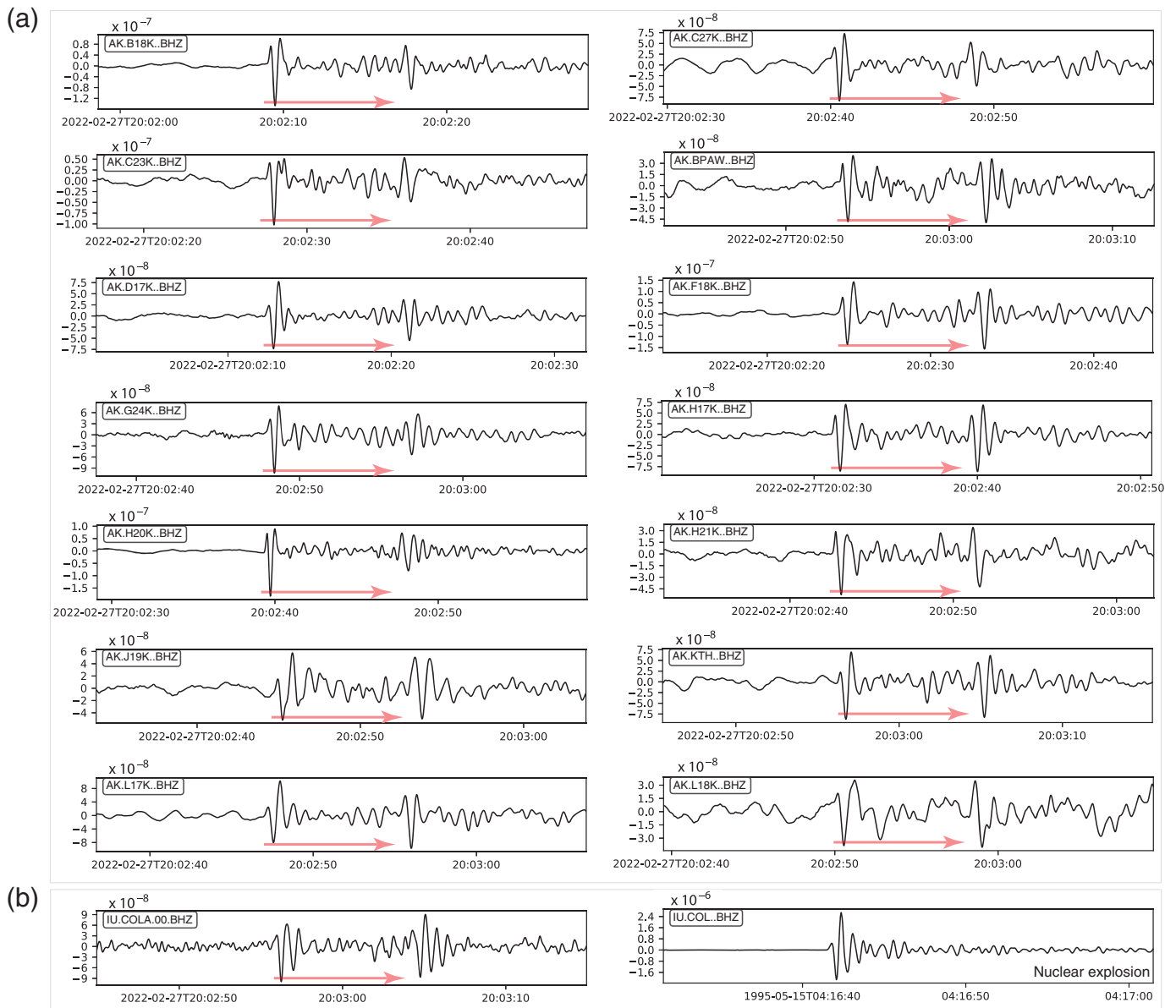
robust low detection threshold for this source region. The 2022 event was not recorded well on stations in Europe or Australia, and was also poorly recorded on most stations of the IC network in China, although we note that recordings of Lop Nor nuclear tests are not available on these stations.

We exploit arrival time data and accurate location estimates of Lop Nor nuclear tests together with the Bayesloc probabilistic multiple event location algorithm to increase confidence in the 2022 event location estimate. Applying strong prior constraints on the nuclear test locations based on highly precise and accurate GT locations shifts the 2022 event estimates several km to the southwest. A joint Bayesloc location with the GT

Figure 5. (a) Recordings of the 2022 event at various stations of the AK network in Alaska. (b) Recordings of the 2022 event on station IU.COLA and of the 15 May 1995 nuclear explosion recorded on the nearby station IU.COL. All waveforms band-pass filtered in the frequency band 1.0–3.5 Hz and all panels display 30 s of data, starting approximately 10 s prior to the *P*-wave arrival pick. The red arrows indicate a duration of 8.0 s.

explosions gives an epicenter of approximately 41.88° N and 88.10° E, close to the location estimates from the Russian Academy of Sciences, Moscow, and IDC in Vienna. A moment tensor inversion indicates a reverse thrust faulting mechanism

with a strike consistent with earthquakes recorded previously in the region (e.g., Selby *et al.*, 2005). The northwest–southeast angle of strike means that stations in these directions are likely to receive little radiated energy, which could explain the poorer *P*-wave detectability in Europe and Australia. A Lop Nor event with a more isotropic source would likely be recorded well in these parts of the world. The inversion indicates a centroid depth of between 18 and 25 km, which is supported further by the observation of likely depth phases recorded on many stations in northern Alaska. Accurate characterization is not only important for discrimination, it will provide an important baseline comparison for subsequent events in this region, potentially at lower magnitudes.

Data and Resources

All waveforms were obtained via the Incorporated Research Institutes for Seismology (IRIS) http://ds.iris.edu/Seismi Query/ (last accessed April 2022). We gratefully acknowledge the operators of the following seismic networks: AK, CN, G IC, II, IM, IU, KN, and KR. The Bayesloc software was obtained from https://www.gs.llnl.gov/nuclear-threat-reduction/nuclear-explosion-monitoring/bayesloc (last accessed April 2022). The National Earthquake Information Center earthquake report for the 27 February 2022 event is found on https://earthquake.usgs.gov/earthquakes/eventpage/us6000h0k8/executive (last accessed April 2022). The hillshade map used to highlight topographic features displayed in Figure 3 was obtained from https://gws-access.jasmin.ac.uk/public/nceo_geohazards/LiCSAR_pro ducts/41/041A_04785_131313/metadata/ (last accessed April 2022). All information from the International Seismological Center (ISC) was obtained via www.isc.ac.uk/iscbulletin/ (ISC, 2022). The Earth3D model and software were obtained via https://www.gs.llnl.gov/nuclear-threat-reduction/nuclear-explo sion-monitoring/global-3d-seismic-tomography (last accessed April 2022). Output from the ISC event search and all the input files needed to run the Bayesloc program to locate this event are found on 10.5281/zenodo.6470585.

Declaration of Competing Interests

The authors acknowledge that there are no conflicts of interest recorded.

Acknowledgments

References

Busby, R. W., and K. Aderhold (2020). The Alaska transportable array: As built, *Seismol. Res. Lett.* doi: 10.1785/0220200154.

Cong, L., J. Xie, and B. J. Mitchell (1996). Excitation and propagation of Lg from earthquakes in central Asia with implications for explosion/earthquake discrimination, *J. Geophys. Res.* **101,** doi: 10.1029/96jb02657.

Dreger, D. S., and D. V. Helmberger (1993). Determination of source parameters at regional distances with three-component sparse network data, *J. Geophys. Res.* **98,** 8107–8125, doi: 10.1029/93JB00023.

Dziewonski, A. M., T. A. Chou, and J. H. Woodhouse (1981). Determination of earthquake source parameters from waveform data for studies of global and regional seismicity, *J. Geophys. Res.* **86,** 2825–2852, doi: 10.1029/jb086ib04p02825.

Ekström, G., A. M. Dziewoński, N. N. Maternovskaya, and M. Nettles (2005). Global seismicity of 2003: Centroid-moment-tensor solutions for 1087 earthquakes, *Phys. Earth Planet. In.* **148,** 327–351, doi: 10.1016/j.pepi.2004.09.006.

Fisk, M. D. (2002). Accurate locations of nuclear explosions at the Lop Nor test site using alignment of seismograms and IKONOS satellite imagery, *Bull. Seismol. Soc. Am.* **92,** 2911–2925, doi: 10.1785/0120010268.

Fox, B. D., N. D. Selby, R. Heyburn, and J. H. Woodhouse (2012). Shallow seismic source parameter determination using intermediate-period surface wave amplitude spectra, *Geophys. J. Int.* **191,** 601–615, doi: 10.1111/j.1365-246X.2012.05612.x.

Hudson, J. A., R. G. Pearce, and R. M. Rogers (1989). Source type plot for inversion of the moment tensor, *J. Geophys. Res.* **94,** 765–774, doi: 10.1029/JB094iB01p00765.

ISC (2022). International Seismological Center Online Bulletin, doi: 10.31905/D808B830.

Jost, M. L., and R. B. Herrmann (1989). A student's guide to and review of moment tensors, *Seismol. Res. Lett.* **60,** 37–57, doi: 10.1785/gssrl.60.2.37.

Kennett, B. L. N., E. R. Engdahl, and R. Buland (1995). Constraints on seismic velocities in the Earth from travel times, *Geophys. J. Int.* **122,** 108–124, doi: 10.1111/j.1365-246x.1995.tb03540.x.

Kohl, B., R. North, J. R. Murphy, M. Fisk, and G. Beall (2002). Demonstration of advanced concepts for nuclear test monitoring applied to the Nuclear Test Site at Lop Nor China, *Proc. of the 24th Seismic Research Review: Nuclear Explosion Monitoring: Innovation and Integration*, Ponte Vedra Beach, Florida, 17–19 September 2002 *Rept. LA-UR-02-5048*, 302–312, available at http://www.ldeo.columbia.edu/res/pi/Monitoring/Doc/Srr_2002/screen/02-08.pdf.

Korrat, I. M., A. A. Gharib, K. A. Abou Elenean, H. M. Hussein, and M. N. El Gabry (2008). Spectral characteristics of natural and artificial seismic events in the Lop Nor test site, China, *Acta Geophys.* **56,** 344–356, doi: 10.2478/s11600-008-00012-3.

Kværna, T., and F. Ringdal (2013). Detection capability of the seismic network of the international monitoring system for the comprehensive Nuclear-Test-Ban Treaty, *Bull. Seismol. Soc. Am.* **103,** 759–772, doi: 10.1785/0120120248.

Kværna, T., S. J. Gibbons, and S. P. Näsholm (2021). CTBT seismic monitoring using coherent and incoherent array processing, *J. Seismol.* **25,** 1189–1207, doi: 10.1007/s10950-021-10026-z.

Lazeckỳ, M., K. Spaans, P. J. González, Y. Maghsoudi, Y. Morishita, F. Albino, J. Elliott, N. Greenall, E. Hatton, A. Hooper, *et al.* (2020). LiCSAR: An automatic InSAR tool for measuring and monitoring tectonic and volcanic activity, *Remote Sens.* **12,** doi: 10.3390/RS12152430.

Levshin, A. L., and M. H. Ritzwoller (1995). Characteristics of surface waves generated by events on and near the Chinese nuclear test site, *Geophys. J. Int.* **123,** 131–148, doi: 10.1111/j.1365-246X.1995.tb06666.x.

Minson, S. E., and D. S. Dreger (2008). Stable inversions for complete moment tensors, *Geophys. J. Int.* **174,** 585–592, doi: 10.1111/j.1365-246X.2008.03797.x.

Myers, S. C., G. Johannesson, and W. Hanley (2007). A Bayesian hierarchical method for multiple-event seismic location, *Geophys. J. Int.* **171,** 1049–1063, doi: 10.1111/j.1365-246x.2007.03555.x.

Myers, S. C., G. Johannesson, and W. Hanley (2009). Incorporation of probabilistic seismic phase labels into a Bayesian multiple-event seismic locator, *Geophys. J. Int.* **177,** 193–204, doi: 10.1111/j.1365-246x.2008.04070.x.

Myers, S. C., N. A. Simmons, G. Johannesson, and E. Matzel (2015). Improved regional and teleseismic P- wave travel-time prediction and event location using a global 3D velocity model, *Bull. Seismol. Soc. Am.* **105,** 1642–1660, doi: 10.1785/0120140272.

Richards, P., F. Waldhauser, D. Schaff, and W.-Y. Kim (2006). The applicability of modern methods of earthquake location, *Pure Appl. Geophys.* **163,** 351–372, doi: 10.1007/s00024-005-0019-5.

Ringdal, F. (1990). Teleseismic event detection using the NORESS array, with special reference to low-yield semipalatinsk explosions, *Bull. Seismol. Soc. Am.* **80,** 2127–2142, doi: 10.1785/BSSA08006B2127.

Saikia, C. K. (1994). Modified frequency-wavenumber algorithm for regional seismograms using Filon's quadrature: Modelling of Lg waves in eastern North America, *Geophys. J. Int.* **118,** 142–158, doi: 10.1111/j.1365-246x.1994.tb04680.x.

Schweitzer, J., and T. Kvaerna (1999). Influence of source radiation patterns on globally observed short-period magnitude estimates (mb), *Bull. Seismol. Soc. Am.* **89,** 342–347, doi: 10.1785/BSSA0890020342.

Selby, N. D., D. Bowers, A. Douglas, R. Heyburn, and D. Porter (2005). Seismic discrimination in southern Xinjiang: The 13 March 2003 Lop Nor earthquake, *Bull. Seismol. Soc. Am.* **95,** 197–211, doi: 10.1785/0120040040.

Waldhauser, F., D. Schaff, P. G. Richards, and W.-Y. Kim (2004). Lop Nor revisited: Underground nuclear explosion locations, 1976-1996, from double-difference analysis of regional and teleseismic data, *Bull. Seismol. Soc. Am.* **94,** 1879–1889, doi: 10.1785/012003184.